

See discussions, stats, and author profiles for this publication at: <https://www.researchgate.net/publication/275524945>

Plasmon-Induced Optical Anisotropy in Hybrid Graphene-Metal Nanoparticle Systems

ARTICLE in NANO LETTERS · APRIL 2015

Impact Factor: 13.59 · DOI: 10.1021/acs.nanolett.5b00789 · Source: PubMed

CITATION

1

READS

275

11 AUTHORS, INCLUDING:



[Adam Gilbertson](#)

Imperial College London

42 PUBLICATIONS 262 CITATIONS

[SEE PROFILE](#)



[Yan Francescato](#)

Imperial College London

19 PUBLICATIONS 362 CITATIONS

[SEE PROFILE](#)



[Vincenzo Giannini](#)

Imperial College London

66 PUBLICATIONS 1,870 CITATIONS

[SEE PROFILE](#)



[Rupert F Oulton](#)

Imperial College London

92 PUBLICATIONS 3,113 CITATIONS

[SEE PROFILE](#)

Plasmon-Induced Optical Anisotropy in Hybrid Graphene–Metal Nanoparticle Systems

Adam M. Gilbertson,^{*,†} Yan Francescato,[†] Tyler Roschuk,[†] Viktoryia Shautsova,[†] Yiguo Chen,^{†,‡} Themistoklis P. H. Sidiropoulos,[†] Minghui Hong,[‡] Vincenzo Giannini,[†] Stefan A. Maier,[†] Lesley F. Cohen,[†] and Rupert F. Oulton^{*,†}

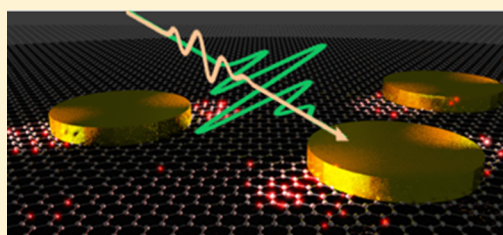
[†]Blackett Laboratory, Imperial College London, Prince Consort Road, London SW7 2BZ, United Kingdom

[‡]Department of Electrical and Computer Engineering, National University of Singapore, 4 Engineering Drive, 117576 Singapore

S Supporting Information

ABSTRACT: Hybrid plasmonic metal–graphene systems are emerging as a class of optical metamaterials that facilitate strong light–matter interactions and are of potential importance for hot carrier graphene-based light harvesting and active plasmonic applications. Here we use femtosecond pump–probe measurements to study the near-field interaction between graphene and plasmonic gold nanodisk resonators. By selectively probing the plasmon-induced hot carrier dynamics in samples with tailored graphene–gold interfaces, we show that plasmon-induced hot carrier generation in the graphene is dominated by direct photoexcitation with minimal contribution from charge transfer from the gold. The strong near-field interaction manifests as an unexpected and long-lived extrinsic optical anisotropy. The observations are explained by the action of highly localized plasmon-induced hot carriers in the graphene on the subresonant polarizability of the disk resonator. Because localized hot carrier generation in graphene can be exploited to drive electrical currents, plasmonic metal–graphene nanostructures present opportunities for novel hot carrier device concepts.

KEYWORDS: Graphene, plasmonic, hybrid, hot carrier, pump–probe, anisotropy



Graphene is attracting considerable interest for optoelectronic applications due to its unique broadband light absorption, electrical tunability, and ease of synthesis that enables straightforward integration with other materials.^{1,2} While its 2D nature is the origin of its remarkable properties, its atomic thickness limits its interaction with light. Consequently, there is considerable interest in hybrid composites of graphene and optically active nanomaterials, such as semiconductor quantum dots (QD), nanowires, and metallic nanoparticles (NPs), that increase the light–matter interaction and extend the functionality of graphene-based optoelectronic devices.^{3–6} Perhaps the most versatile of these are the metal–graphene hybrids that exploit the near-field coupling between graphene carriers and surface plasmon (SP) excitations supported in metal NPs. The ability of graphene to control the SP resonance of metallic nanostructures has been demonstrated as a platform for gigahertz optical modulation^{7,8} and attomolar biomolecule detection in SP resonance spectroscopy.⁹ Meanwhile, metallic NPs act as antennas that concentrate light into nanoscopic volumes via the excitation of their localized SP resonance that promote strong photoabsorption in the graphene layer, as well as efficient launching of graphene plasmons.¹⁰ Several groups have reported an enhanced photoresponse in plasmonic metal–graphene hybrids.^{3,6,11,12} However, a complete understanding of how the near-field interactions between graphene and

plasmonic NPs contribute to hot carrier generation and relaxation processes in the graphene is so far lacking.

Central to the physics of plasmonic metal–graphene hybrids are plasmon-induced hot carriers generated in the graphene via the intense electromagnetic fields surrounding the NP (direct photoexcitation) and within the NP via nonradiative plasmon decay.¹³ The latter process can be quite efficient in small NPs¹⁴ and has stimulated broad interest in plasmonic energy conversion because these hot carriers can be emitted from the NP into a suitable collector and be harvested, for example, to extend the band gap spectral limit in semiconductor photovoltaic devices.¹⁵ Hot carrier transfer across the metal–graphene interface is appealing at a conceptual level due to the gapless band structure of graphene, making it a highly efficient hot electron collector.¹⁶ However, the absence of an energy barrier means that back transfer from the graphene to the NP may be just as favorable, limiting the overall contribution of the charge transfer process to the photoinduced response of graphene.

In this Letter, we report the plasmon-induced hot carrier dynamics of a hybrid metal–graphene system consisting of plasmonic nanodisk resonators coupled to a graphene over-

Received: February 26, 2015

Revised: April 10, 2015

layer. Nanodisks are an ideal test structure due to their ease of fabrication that allows close packing and readily tunable dipole resonance that couples strongly to the far-field. By selectively probing the photocarrier dynamics in the graphene layer, following excitation at the SP band of the NP array, we gain direct access to the influence of graphene–NP interactions on the transient hot carrier population in the graphene. In order to distinguish between plasmon-induced hot carrier generation processes we compare samples where graphene is in direct contact with the metal NP (sample A) to those in which a hexagonal boron nitride (BN) monolayer has been introduced at the graphene–metal interface (sample B), shown schematically in Figure 1a. The BN spacer layer serves as an effective

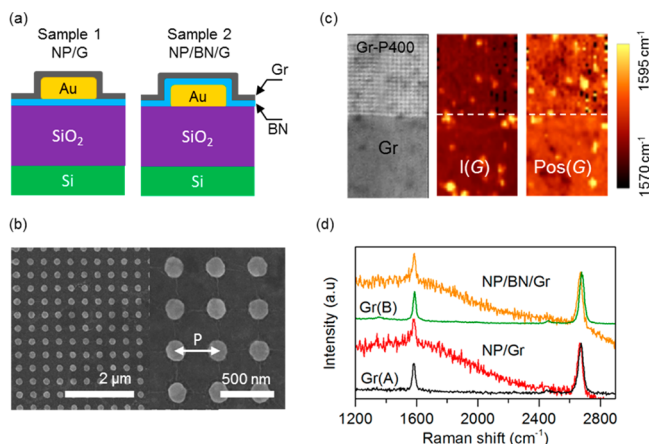


Figure 1. Sample design and characterization. (a) Schematic cross sections of sample A (gold/Gr interfaces) and sample B (gold/BN/Gr interfaces). (b) An SEM image of a gold nanodisk array (disk diameter 200 nm and lattice period $P = 400$ nm) with graphene overlay (sample A). (c) Micro-Raman mapping: $7.5 \mu\text{m} \times 15 \mu\text{m}$ optical image (left) and corresponding spatial maps of the graphene G-band intensity (middle) and position, Pos(G) , from sample A are shown in Figure 1c and demonstrate the uniform coverage. (d) Representative Raman spectra of the bare graphene and graphene–NP structure from samples A and B indicating almost identical properties of the graphene (532 nm excitation, 1 mW).

barrier to charge transfer,¹⁷ while being just angstroms thick it has little effect on the plasmon-mediated electromagnetic field intensity at the graphene (verified by numerical simulations). We demonstrate that direct near-field photoexcitation is the dominant process for plasmon-induced hot carrier generation in the graphene and gives rise to a strong optical anisotropy in the hybrid samples, absent in bare graphene and NP control samples, as revealed by polarization-resolved measurements. Intrinsic optical anisotropy, driven by the preferential occupation of specific states in k -space through to the carrier-field interaction, is known to occur in various semiconductors^{18–20} including graphene²¹ but is generally short-lived due to fast carrier-phonon scattering (~ 100 fs) that redistributes the photocarrier momentum. Here we show that the strong optical near-field coupling of graphene to plasmonic NPs underpins a long-lived extrinsic optical anisotropy. The effect arises from the action of highly localized hot carriers in the graphene on the subresonant NP polarizability and persists for several hundred fs, determined by the diffusion of hot carriers away from hot-spots. Our observations highlight the rich physics associated with the graphene–NP interaction, and the

potential to exploit plasmonic metal–graphene nanostructures in photothermoelectric applications.

Gold nanodisk arrays extending over an area of $40 \mu\text{m} \times 40 \mu\text{m}$ were fabricated using e-beam lithography, thermal evaporation (40 nm gold) and lift-off. The graphene and monolayer BN were grown by chemical vapor deposition and deposited using a dry transfer technique.²² A representative SEM image of the nanostructures is shown in Figure 1b. Nanodisks with a diameter (d) of 200 nm were chosen to give a localized SP resonance in the near-IR region, far from gold's interband transitions.²³ Several arrays were fabricated with lattice periods (P) ranging between 400 and 1000 nm. We focus our discussions on the results from the $P = 400$ nm arrays (Figure 1b) that exhibit the strongest plasmonic response. The transferred graphene was characterized by micro-Raman spectroscopy that indicates the almost identical properties of the two samples (see Figure 1d). The Raman spectra of bare graphene regions are indicative of monolayer graphene with relatively low doping (obtained by employing a dry transfer method and BN support layer which passivates the SiO_2 surface²⁴). From the average position of the G-band we estimate a chemical potential $\mu \approx 0.2\text{--}0.3$ eV.^{25,26} Over the NP array, the graphene Raman bands are superimposed on a broad background fluorescence from the gold. Notably, the absence of a significant shift in the average G-band position when on and off the arrays implies minimal change in the chemical potential of graphene over the NPs. Spatial maps of the graphene G-band intensity, $I(\text{G})$, and position, Pos(G) , from sample A are shown in Figure 1c and demonstrate the uniform coverage. Similar results are obtained from sample B.

Figure 2a shows the measured reflectance spectra of the samples exhibiting a resonant feature around 700 nm–800 nm. The experimental data show excellent agreement with the simulated spectrum obtained using the finite element method described in ref 27 taking into account the Si/SiO₂ substrate (Supporting Information). Figure 2b shows the simulated near-field intensity enhancement spectrum, $f_{\text{NF}}(\lambda)$, (2 nm outside

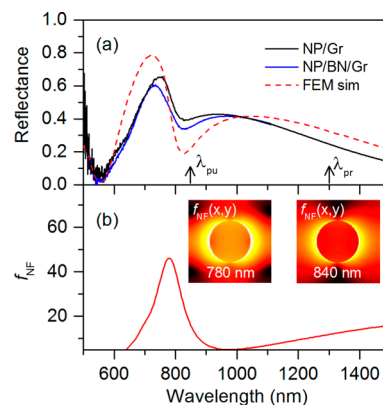


Figure 2. Plasmonic response of the graphene-nanodisk array. (a) Measured reflectance spectra of the graphene-NP array ($P = 400$) from sample A (solid black line) and B (solid blue line) with p-polarized light. The simulated reflectance spectrum is shown by the red dashed line. The pump (λ_{pu}) and probe (λ_{pr}) used in the time-resolved measurements are indicated by the arrows. (b) Calculated near-field intensity enhancement f_{NF} as a function of incident wavelength indicating the SP resonance at ~ 780 nm. Inset: Near-field intensity enhancement distribution $f_{\text{NF}}(x,y)$ of a gold nanodisk excited with x-polarized light at 780 and 840 nm illustrating the dipole mode of the SP resonance (log scale from 0.1 (black) to 100 (yellow)).

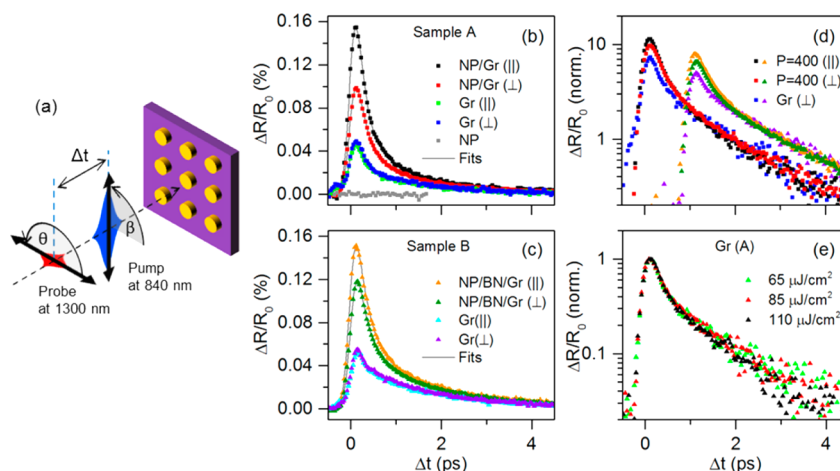


Figure 3. Time-resolved carrier dynamics. (a) Schematic illustration of the pump–probe measurement geometry; Polarization angles are measured with respect to the plane of incidence; Δt is the pump–probe delay. (b,c) Differential reflection $\Delta R/R_0$ as a function of Δt for bare graphene (Gr) and the hybrid structures from sample A and B measured with parallel (||) and perpendicular (\perp) pump and probe polarizations. No signal is measured from the NP array without a graphene overlayer (gray dots). Solid lines show fits to a biexponential decay convoluted with a Gaussian (fwhm = 260 fs). (d) $\Delta R/R_0$ transients normalized to the value at $\Delta t = 2$ ps on a semilog plot showing similar cooling rates at long time delays and distinct changes to the heating efficiency in the hybrid structures (data for sample B is shifted by 1 ps for clarity). (e) Effect of varying pump fluence on the bare graphene (\perp) cooling dynamics. Data are normalized to their maximum and collapse onto the same curve indicating that the initial carrier temperature does not affect the dynamics in the range of the pump fluence considered.

the NP) indicating the localized SP resonance of the NP array at ~ 780 nm. The dipolar mode of the resonance is shown by the near-field distributions, $f_{\text{NF}}(x, y)$, in the inset to Figure 2b (note log scale). We note that the cylindrical symmetry of an ideal disk gives a polarization-independent plasmonic response; however, the real disks in our experiments exhibit a slight ($\sim 5\%$) geometric ellipticity which manifests as an ~ 20 nm shift in the localized SP resonance for s -polarized and p -polarized light (Supporting Information). This is similar in magnitude to the sample to sample variation seen in Figure 2a and does not influence the transient anisotropy reported in this letter.

To study the plasmon-induced hot carrier dynamics in graphene we perform time-resolved differential reflection (DR) measurements (see Experimental Methods). Samples are optically excited with linearly polarized 200 fs pump pulses centered at 840 nm (coinciding with the localized SP band of the NP array) and probed at 1300 nm with varying delay and polarization with respect to the pump (see Figure 3a). The near-IR pump pulse excites hot carriers in graphene through direct interband absorption. In the gold, hot conduction electrons are generated by strong free carrier absorption at the localized SP band of the NPs (note that the coherent surface plasmon lifetime in gold is typically less than 20 fs and can be ignored in our discussion²³). Immediately following photoexcitation, the strongly out-of-equilibrium photocarriers in both materials rapidly thermalize with ambient carriers in the Fermi sea forming a hot carrier distribution. The transient DR is then connected to an excited state characterized by a well-defined electronic temperature (T_{el}), greatly exceeding that of the lattice.^{28,29} In graphene, the occupation of states in the extended tail of the hot carrier distribution produces a DR signal for a wide range of probe energies. Meanwhile, the rapid electronic heating of NPs results in a broadening and redshift of their scattering spectrum²³ yielding a large DR signal for probe energies close to the localized SP band. Previous measurements on hybrid structures have used the latter approach and are typically dominated by the NP response.^{12,30} The use of a widely separated probe energy, reported here, is essential in

order to separate the plasmon-induced graphene response of interest from the nonlinear response of the NPs.

Initially, DR measurements were performed on the NP array prior to graphene transfer. The observation of a null response, as indicated by the gray symbols in Figure 3a, confirms that the probe is insensitive to the nonlinear response of the NPs. A DR signal is only observed when graphene is present. To examine the impact of the plasmonic NP array we directly compare the measured dynamics in the hybrid structures to those of bare graphene. The DR transients from samples A and B obtained with parallel (||) and cross-polarized (\perp) pump and probe beams are shown in Figure 3b, and c, respectively. The transient behavior of both samples is qualitatively the same: the bare graphene areas of each sample exhibit a positive DR signal decaying on a time scale of several picoseconds, similar to previous two-color pump–probe studies of graphene.^{31,32} No dependence on the pump and probe polarizations is observed within the experimental error. In contrast, the graphene–NP structures exhibit an increased DR signal with a pronounced dependence on the relative pump and probe polarizations. The large NP-induced anisotropic response is surprising and is discussed in detail later.

Key insight into the influence of the graphene–NP interaction on the graphene hot carrier population is gained from examining the peak DR signal ($\Delta R_{\text{max}}/R_0$) that is directly connected to the peak hot carrier temperature (Table 1). The increased peak DR observed in the graphene–NP structures demonstrates enhanced hot carrier generation in the graphene layer. From closer inspection of Figure 3b,c we find that the average (isotropic) part of the DR response, $\chi = (\Delta R^{(\text{||})}/R_0 + \Delta R^{(\text{⊥})}/R_0)/2$, from the graphene/NP and graphene/BN/NP structures is essentially the same. Given the low tunneling probability of the graphene/BN interface¹⁷ $\approx 20\%$ and the anticipated impact on charge transfer, this observation indicates that the dominant mechanism for plasmon-induced hot carrier generation in the graphene originates from the near-field enhancement of direct photoexcitation in the graphene, rather than hot carrier transfer from the nanodisks.

Table 1. Decay Parameters for the DR Transients Shown in Figures 3b,c: τ_2 and A_2 are the Decay Rate and Extrapolated Amplitude of the Secondary Decay Component Associated with Hot-Phonons^a

sample	$\Delta R_{\max}/R_0$ (%)	τ_2 (ps)	A_2 (%)	A_1/A_2^*
A: Gr/NP (\parallel)	0.154	1.58	0.043	1.52
A: Gr/NP (\perp)	0.099	1.73	0.032	1.31
A: Gr	0.049	1.79	0.021	1
B: Gr/hBN/NP (\parallel)	0.151	1.77	0.062	1.52
B: Gr/hBN/NP (\perp)	0.118	1.80	0.054	1.36
B: Gr	0.047	1.78	0.029	1

^aThe ratio A_1/A_2^* is normalised to value of bare graphene in each sample.

The relaxation dynamics in bare graphene and graphene–NP structures exhibit two distinct time scales: an initial fast decay (τ_1), followed by a slower secondary decay (τ_2) at later delays. This biexponential behavior has been widely reported in graphene and is attributed to a hot phonon bottleneck effect where the two time scales result from relaxation processes involving optical phonons and acoustic phonons, respectively.^{31,33} To compare the dynamics more clearly, in Figure 3d the data is normalized to the value at $\Delta t = 2$ ps when the secondary decay is dominant (data for sample B is shifted by 1 ps for clarity). Notably, the graphene and graphene–NP data from each sample collapse onto the same secondary decay curves ($\Delta t > 1$ ps) with a similar characteristic decay constant of $\tau_2 \approx 1.7$ ps (see Table 1). This indicates that the rate-limiting energy dissipation process in graphene, presumably involving acoustic phonons, is unaffected by coupling to the gold NP array. This agrees with Raman studies on graphene–gold interfaces reported in ref 26 and provides further evidence for the robust carrier-phonon coupling in graphene.

The effect of graphene–NP coupling on the carrier dynamics is clearly revealed at short time delays as a marked increase in amplitude of the initial decay component relative to that in bare graphene (Figure 3d). While this is a clear indication of plasmon-induced changes to the initial hot carrier excitation-

relaxation pathways in the graphene, the limited time resolution of our measurement (~ 260 fs) does not permit a more detailed quantitative analysis.

During the early stages of relaxation, thermalized hot carriers rapidly dissipate the majority of their energy via emission of optical phonons, which in turn raises the temperature of the optical phonon subsystem (T_{ph}): when $T_e \approx T_{ph}$, the dynamics of the carrier and phonon systems become closely coupled and the anharmonic decay of hot optical phonons into acoustic phonons forms the main bottleneck for subsequent cooling.^{31,33} Accordingly, we find the carrier dynamics in both samples are well described by a biexponential decay model of the form $\Delta R(\Delta t) \propto A_1 e^{-(\Delta t)/\tau_1} + A_2 e^{-(\Delta t)/\tau_2}$, as shown by the solid lines in Figure 3b,c. Proceeding with the analysis, the amplitudes associated with the initial and secondary decay components are connected to the peak hot carrier and hot-phonon temperatures in the graphene, respectively. The amplitude ratio A_1/A_2 that characterizes the overall shape of the dynamics (Figure 3d,e) is proportional to the temperature ratio T_e/T_{ph} and therefore provides a useful qualitative indication of the fraction of energy lost to the phonons during the heating process. This characteristic shape of the dynamics is independent of the incident pump fluence (and hence, initial T_e in the graphene) over a wide range as shown in Figure 3e, where DR transients for bare graphene obtained at higher pump fluences collapse onto the same normalized curve. The heating efficiency in graphene is determined by the competition between inelastic phonon scattering and elastic carrier–carrier scattering during the thermalization process:³⁴ efficient carrier heating implies fast carrier–carrier scattering that can lead to hot carrier multiplication³⁵ with implications for energy-harvesting applications.

To quantify this fraction we compare the measured peak DR signal ($\sim A_1$) with the value $A_2 \approx \Delta R/R_0(2)e^{2/\tau_2}$ extrapolated from the DR signal at $\Delta t = 2$ ps and secondary decay rate associated with hot-phonons (shown in Table 1). The fact that this ratio is enhanced in the graphene–NP structures may be viewed as a signature of increased carrier heating efficiency.

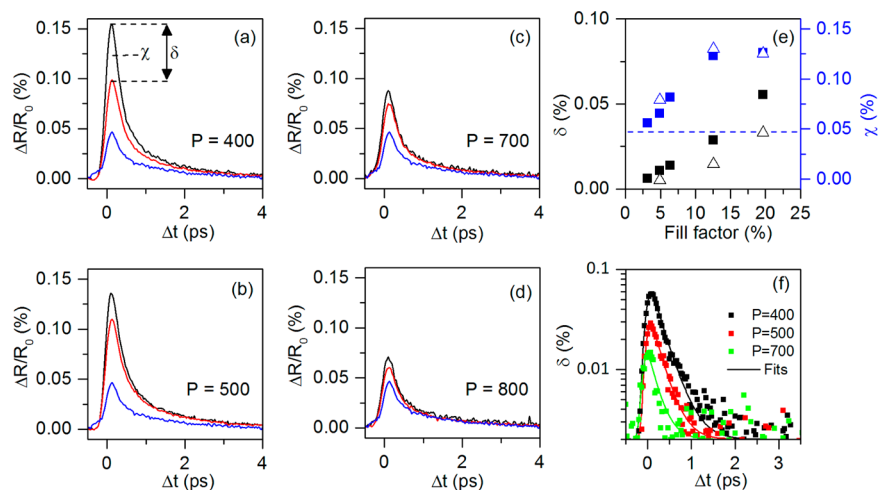


Figure 4. Influence of graphene–nanoparticle coupling. (a–d) Differential reflection transients for hybrid graphene/NP structures (sample A) with varying NP lattice periods (P) obtained with parallel (black line) and perpendicular (red line) pump–probe polarizations. The response of bare graphene is shown by the blue lines for comparison. The average (isotropic) part (χ) and anisotropic part (δ) of the signal are defined in (a). (e) Dependence of δ and χ on the metal fill factor of the NP arrays for sample A (closed symbols) and sample B (open symbols). The blue dashed line represents the bare graphene signal amplitude. (f) Temporal evolution of δ for varying P (sample A). Solid lines are fits to a single exponential decay convoluted with a Gaussian (fwhm = 260 fs).

Taking into account sample to sample variation by normalizing to the ratio deduced for bare graphene, we find that the relative increase in the DR amplitude ratio is approximately the same in both the graphene/NP and graphene/hBN/NP structures. This reinforces our assertion that charge transfer plays a minimal role in the hot carrier dynamics of our samples.

Next, we focus on the transient anisotropy observed in the graphene–NP structures. The contribution of the graphene–NP interaction to the anisotropic response is elucidated by examining the influence of NP density. Figure 4a–d shows DR transients from NP arrays with varying lattice periods (P), from sample A. The amplitude of the anisotropic part of the signal, defined as $\delta = \Delta R^{(||)}/R_0 - \Delta R^{(\perp)}/R_0$, and the average (isotropic) part, χ , both reduce with increasing P . Figure 4e shows that δ is in fact directly proportional to the geometrical nanodisk filling factor $g = (\pi d^2)/(4p^2)$. Meanwhile, χ appears to saturate for $g > 10\%$, which is attributed to the interplay between average enhancement of photoexcitation and NP coverage. Finally, we find that δ decays with a characteristic time constant of $\tau_\delta \sim 300$ fs, independent of P (see Figure 4f). Combined, these results clearly demonstrate that the isotropic and anisotropic responses of the hybrid structure are determined entirely by the interaction of graphene with individual nanodisks within the array.

Before discussing the physical origins of the anisotropy, we present the polarization dependence in more detail. Figure 5a

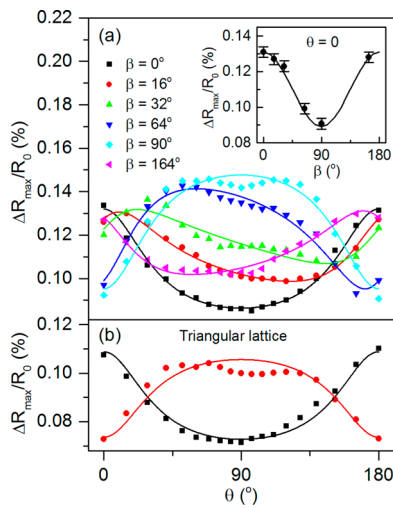


Figure 5. Optical anisotropy of the graphene-nanoparticle system. (a) Dependence of the DR amplitude ($\Delta R_{\max}/R_0$) on the probe polarization angle θ for a graphene/NP structure (sample A) with square lattice. Solid lines are two parameter fits according to eq 1. Inset: $\Delta R_{\max}/R_0$ versus β for $\theta = 0$, demonstrating a $\cos(2\beta)$ dependence expected from the model (see text). The solid line is obtained from eq 1. (b) Measurements from an equivalent NP array with a triangular lattice display the same symmetry as in (a), confirming the absence of lattice effects.

shows the dependence of the peak DR signal ($\Delta R_{\max}/R_0$) on probe polarization angle θ for sample A, at several fixed values of β (see Figure 3a). No dependence on the sample orientation was found (not shown). A pump-induced anisotropic DR response should follow a $\cos 2(\beta - \theta)$ variation, equivalent to Malus' law (Supporting Information); however, the data in Figure 5a show a notable departure from this simple prediction. Additional measurements performed on a separate sample with triangular lattice nanodisk arrays display the same polarization

dependence (see Figure 5b), confirming the absence of lattice effects.

To interpret our data, we must account for the collinear reflection geometry of our apparatus and the use of a beam splitter to direct the reflected probe beam to the photodetector. Taking into account the contribution of pump-induced polarization rotations of the probe beam (due to the sample anisotropy) to the reflected signal from the beam splitter, the polarization dependence of the DR signal for our experiment is given by

$$\frac{\Delta R_{\max}}{R_0}(\theta, \beta) = A^2 - 1 + 2AB \frac{(A_R \cos(2\beta) + \cos(2(\beta - \theta)))}{(1 + A_R \cos(2\theta))} \quad (1)$$

Where $A = (1 + \chi)^{1/2}$, $B \approx \delta/(1 + \chi)^{1/4}$ and $A_R = -0.55$ is a constant that characterizes the anisotropy of the beam splitter. Details of the model are given in Supporting Information. The solid lines in Figure 4a are obtained from eq 1 and show excellent agreement with the data using the two parameters A and B obtained from the experiments. For $\theta = 0^\circ$, the variation of $\Delta R_{\max}/R_0$ with β is given by $\cos(2\beta)$, as demonstrated in the inset to Figure 5a, where the solid line is obtained from eq 1 using $A^2 - 1 = 0.11\%$ and $2AB = 0.02\%$. The relative strength of the anisotropy, given by $B/(A - 1)$, is found to be $\sim 15\%$ of the pump-induced change in sample reflectivity and corresponds to a maximum polarization rotation of $\Delta\theta \approx 0.01^\circ$ (when $\beta - \theta = 45^\circ$). We note that although this value is rather small, it reflects the weak interaction of light with monolayer graphene. Indeed, considering the nonlinear activity to take place in the graphene, the figure of merit for specific polarization rotation ($\Delta\theta/\text{thickness}/\text{peak intensity}$) $\approx 1 \times 10^{-3} \text{ }^\circ \text{ cm/W}$ is comparable to the strong optical rotations observed in nonlinear plasmonic metamaterials.³⁶

Next we discuss the physical origin of the observed anisotropy. In general, optical excitation of semiconductors with linearly polarized light drives an intrinsic anisotropy that can manifest in pump–probe experiments with sufficient temporal resolution.^{18–20} This effect is caused by the initial anisotropic distribution of photocarriers in k -space that exists momentarily following excitation by the pump pulse and was recently observed in graphene by Mittendorf et al.²¹ using pump–probe measurements with sub 50 fs resolution. It was shown that an isotropic photocarrier distribution is re-established within the first 100–150 fs via rapid carrier-phonon scattering, consistent with theoretical predictions.³⁷ As this momentum randomization is significantly faster than the temporal resolution of our measurement, the contribution from this intrinsic effect can be excluded. This is justified by the absence of anisotropy in the bare graphene samples (Figure 3). In addition, acoustic vibrations in the NP size following excitation (so-called breathing modes) occur on time scales > 10 ps and do not influence the cooling of hot carriers.³⁸

In the following, we present a simple model for optical anisotropy originating from the strong near-field graphene–NP interaction. We ignore charge transfer because, as discussed above, it is not the dominant mechanism for hot carrier generation in our samples. The plasmonic near-field enhancements (inset to Figure 2b) lead to increased photocarrier generation in the graphene as reported by previous groups.^{3,11,39} More precisely, because the local photoabsorption is $\propto f_{\text{NF}}(x, y)$, the nanodisk generates a highly nonuniform

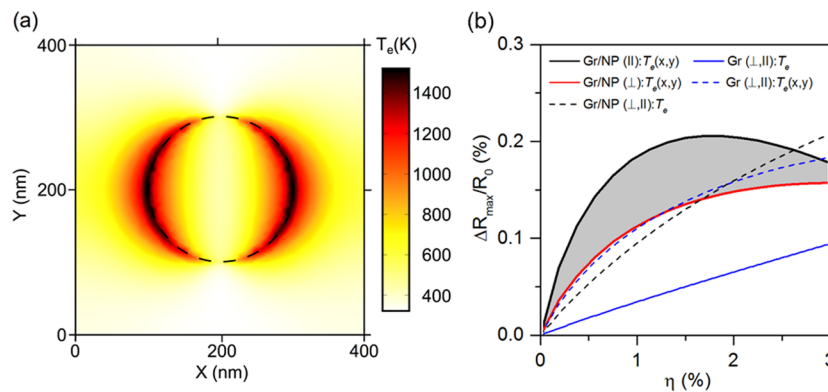


Figure 6. Model for plasmon-induced optical anisotropy. (a) Plasmon-induced electron temperature distribution, $T_e(x,y)$, in the graphene due to near-field carrier heating (dashed line denotes the disk perimeter). $T_e(x,y)$ is calculated for 840 nm pump light polarized in the x -direction, using the experimental fluence and a heating efficiency $\eta = 1.5\%$ (see Experimental Methods). (b) Simulated DR of the graphene/NP structure exhibits strong anisotropy between parallel and perpendicular pump–probe polarizations due to $T_e(x,y)$ (solid black and red lines), emphasized by the shaded region. The anisotropy vanishes for the case of uniform temperature T_e (dashed black line). Bare graphene exhibits an isotropic DR for both uniform (solid blue line) and nonuniform (dashed blue line) temperature distributions.

spatial distribution of hot carriers in the graphene. For simplicity, we assume that the main effect of this is the near-field carrier heating of graphene due to photoexcitation and quasi-instantaneous thermalization.²⁹ To investigate this we perform numerical simulations of the DR according to $\Delta R_{\text{max}}/R_0 = [R(T_e(x,y)) - R(T_{e0})]/R(T_{e0})$. $R(T_{e0})$ and $R(T_e(x,y))$ are the simulated reflectances of the entire structure at 1300 nm using the equilibrium ($T_{e0} = 300$ K), and pump-induced electron temperature distribution in the graphene, respectively. The electron temperature distribution $T_e(x,y)$ is calculated using the $f_{\text{NF}}(x,y)$ distribution simulated at 840 nm (Supporting Information). Following ref 29, we introduce a phenomenological electronic heating efficiency (η) to describe the fraction of absorbed energy retained in the carrier system during the heating process. Note that η only determines the maximum electron temperature in the graphene. An example of $T_e(x,y)$ generated using $\eta = 1.5\%$ is shown in Figure 6a.

Figure 6b shows the DR simulations for the graphene/NP ($P = 400$ nm) structure as a function of η , when the probe field is parallel (solid black curve) and perpendicular (solid red curve) to the pump field. The model produces a significant anisotropy in the hybrid structure and correctly predicts the experimental observations of $\Delta R^{(\parallel)}/R_0 > \Delta R^{(\perp)}/R_0$ for small η . The agreement is quite satisfactory given the simplicity of the model, which neglects any temporal evolution of the hot carrier distribution during the heating process. The simulation of bare graphene (solid blue curve) with uniform T_e (i.e., when $f_{\text{NF}}(x,y) = 1$) shows no polarization dependence as expected. Note that the simulated DR exhibits a nonmonotonic dependence on η due to the sensitivity of interference within the SiO_2 layer to the dielectric properties of graphene (this effect is apparent at lower η in the graphene–NP system due to the field enhancements). The simulations highlight the physical origin of the anisotropy in hybrid samples to be the action of localized plasmon-induced hot carriers in the graphene on the subresonant polarizability of the NP, through the graphene conductivity. This mutual interaction is exemplified by the dashed curves in Figure 6b, where upon removing either the NPs or the nonuniform temperature distribution from the simulation, the anisotropy vanishes.

According to this model the anisotropy will persist as long as the hot electron distribution around the NP remains

anisotropic. This is approximately the time taken for hot carriers to diffuse across the nanodisk diameter given by $\tau_\delta = 4r^2/D_e$, where r is the nanodisk radius and D_e is the hot carrier diffusion coefficient. Taking the value of $\tau_\delta = 300$ fs from our experiment, this yields a hot carrier diffusion coefficient of $D_e \approx 1300$ cm²/s, comparable to that previously reported for CVD graphene.³²

We point out that our results may have interesting technological implications because near-field heating at graphene–metal interfaces could be exploited to drive an electrical current via the large Seebeck coefficient in graphene without the need for symmetry breaking interfaces such as p–n junctions.⁴⁰

In summary, we have used femtosecond pump–probe measurements to study the near-field interaction of graphene with plasmonic nanodisk resonators. Our results indicate that plasmon-induced hot carrier generation in the graphene is dominated by direct photoexcitation through the intense near-fields. The interaction of the plasmon-induced hot carriers in the graphene with the nanodisk polarizability gives rise to a striking and long-lived extrinsic optical anisotropy. In addition to introducing a hybrid nanomaterial with strong optical activity, our results highlight that large electronic temperature gradients can be achieved and exploited in plasmonic metal–graphene systems at the nanoscale.

Experimental Methods. Two-color pump–probe measurements were conducted at room-temperature ambient conditions. A 80 MHz mode-locked Ti:sapphire laser (Coherent Chameleon Ultra II) operating at 840 nm (1.48 eV) provided linearly polarized, nominally 200 fs duration pump pulses. Part of the output is used to pump an optical parametric oscillator (Coherent Chameleon OPO) from which 1300 nm (0.95 eV) probe pulses are obtained. The polarization angle of the pump (β) and probe (θ) beams are measured with respect to the plane of incidence as illustrated in Figure 3a and are controlled independently by two $\lambda/2$ -waveplates. After a mechanical delay stage, pump and probe pulses are aligned through a beam splitter in a collinear geometry and focused onto the sample surface at normal incidence through a microscope objective (0.6 NA Nikon Plan Fluor 40x) yielding spot sizes of 6 and 2 μm , respectively. An incident pump fluence $F \sim 45$ $\mu\text{J}/\text{cm}^2$ (corresponding to a pulse energy of 12.5

pJ) was used for all measurements presented unless stated otherwise. The ratio of the pump to probe fluence was $>10:1$. Reflected probe pulses are detected with an InGaAs photodiode using suitable filters to minimize signal from reflected pump light. The pump beam is modulated at ~ 500 Hz with a mechanical chopper in order to detect the pump-induced change in probe reflectance, $\Delta R = R' - R_0$, with a lock-in amplifier; R' and R_0 are the probe reflectance with and without pump excitation, respectively.

■ ASSOCIATED CONTENT

■ Supporting Information

Further details on the experiment, sample characterization, and numerical calculations. The Supporting Information is available free of charge on the ACS Publications website at DOI: 10.1021/acs.nanolett.5b00789.

■ AUTHOR INFORMATION

Corresponding Authors

*E-mail: a.gilbertson@imperial.ac.uk.

*E-mail: r.oulton@imperial.ac.uk.

Notes

The authors declare no competing financial interest.

■ ACKNOWLEDGMENTS

The authors gratefully acknowledge funding from the EPSRC (EP/K016407/1, EP/J014699/1, EP/H000917/2, EP/I004343/1), the Royal Society and the Leverhulme Trust.

■ REFERENCES

- (1) Bao, Q. L.; Loh, K. P. *ACS Nano* **2012**, *6*, 3677–3694.
- (2) Sun, Z. H.; Chang, H. X. *ACS Nano* **2014**, *8*, 4133–4156.
- (3) Echtermeyer, T. J.; Britnell, L.; Jasnos, P. K.; Lombardo, A.; Gorbachev, R. V.; Grigorenko, A. N.; Geim, A. K.; Ferrari, A. C.; Novoselov, K. S. *Nat. Commun.* **2011**, *2*, 458.
- (4) Konstantatos, G.; Badioli, M.; Gaudreau, L.; Osmond, J.; Bernechea, M.; de Arquer, F. P. G.; Gatti, F.; Koppens, F. H. L. *Nat. Nanotechnol.* **2012**, *7*, 363–368.
- (5) Koppens, F. H. L.; Mueller, T.; Avouris, P.; Ferrari, A. C.; Vitiello, M. S.; Polini, M. *Nat. Nanotechnol.* **2014**, *9*, 780–793.
- (6) Liu, Y.; Cheng, R.; Liao, L.; Zhou, H. L.; Bai, J. W.; Liu, G.; Liu, L. X.; Huang, Y.; Duan, X. F. *Nat. Commun.* **2011**, *2*, 579.
- (7) Yao, Y.; Kats, M. A.; Genevet, P.; Yu, N. F.; Song, Y.; Kong, J.; Capasso, F. *Nano Lett.* **2013**, *13*, 1257–1264.
- (8) Yao, Y.; Kats, M. A.; Shankar, R.; Song, Y.; Kong, J.; Loncar, M.; Capasso, F. *Nano Lett.* **2014**, *14*, 214–219.
- (9) Zagorodko, O.; Spadavecchia, J.; Yanguas Serrano, A.; Larroulet, I.; Pesquera, A.; Zurutuza, A.; Boukherroub, R.; Szunerits, S. *Anal. Chem.* **2014**, *86*, 11211–11216.
- (10) Alonso-Gonzalez, P.; Nikitin, A. Y.; Golmar, F.; Centeno, A.; Pesquera, A.; Velez, S.; Chen, J.; Navickaite, G.; Koppens, F.; Zurutuza, A.; Casanova, F.; Hueso, L. E.; Hillenbrand, R. *Science* **2014**, *344*, 1369–1373.
- (11) Fang, Z. Y.; Liu, Z.; Wang, Y. M.; Ajayan, P. M.; Nordlander, P.; Halas, N. J. *Nano Lett.* **2012**, *12*, 3808–3813.
- (12) Nikolaenko, A. E.; Papasimakis, N.; Atmatzakis, E.; Luo, Z. Q.; Shen, Z. X.; De Angelis, F.; Boden, S. A.; Di Fabrizio, E.; Zheludev, N. I. *Appl. Phys. Lett.* **2012**, *100*, 181109.
- (13) Brongersma, M. L.; Halas, N. J.; Nordlander, P. *Nat. Nanotechnol.* **2015**, *10*, 25–34.
- (14) Govorov, A. O.; Zhang, H.; Gun'ko, Y. K. *J. Phys. Chem. C* **2013**, *117*, 16616–16631.
- (15) Knight, M. W.; Sobhani, H.; Nordlander, P.; Halas, N. J. *Science* **2011**, *332*, 702–704.
- (16) Gaudreau, L.; Tielrooij, K. J.; Prawiroatmodjo, G. E. D. K.; Osmond, J.; de Abajo, F. J. G.; Koppens, F. H. L. *Nano Lett.* **2013**, *13*, 2030–2035.
- (17) Britnell, L.; Gorbachev, R. V.; Jalil, R.; Belle, B. D.; Schedin, F.; Mishchenko, A.; Georgiou, T.; Katsnelson, M. I.; Eaves, L.; Morozov, S. V.; Peres, N. M. R.; Leist, J.; Geim, A. K.; Novoselov, K. S.; Ponomarenko, L. A. *Science* **2012**, *335*, 947–950.
- (18) Sabbah, A. J.; Riffe, D. M. *Phys. Rev. B* **2002**, *66*, 165217.
- (19) Smirl, A. L.; Boggess, T. F.; Wherrett, B. S.; Perryman, G. P.; Miller, A. *IEEE J. Quantum Electron.* **1983**, *19*, 690–700.
- (20) Portella, M. T.; Bigot, J. Y.; Schoenlein, R. W.; Cunningham, J. E.; Shank, C. V. *Appl. Phys. Lett.* **1992**, *60*, 2123–2125.
- (21) Mittendorf, M.; Winzer, T.; Malic, E.; Knorr, A.; Berger, C.; de Heer, W. A.; Schneider, H.; Helm, M.; Winnerl, S. *Nano Lett.* **2014**, *14*, 1504–1507.
- (22) Suk, J. W.; Kitt, A.; Magnuson, C. W.; Hao, Y. F.; Ahmed, S.; An, J. H.; Swan, A. K.; Goldberg, B. B.; Ruoff, R. S. *ACS Nano* **2011**, *5*, 6916–6924.
- (23) Link, S.; El-Sayed, M. A. *J. Phys. Chem. B* **1999**, *103*, 8410–8426.
- (24) Dean, C. R.; Young, A. F.; Meric, I.; Lee, C.; Wang, L.; Sorgenfrei, S.; Watanabe, K.; Taniguchi, T.; Kim, P.; Shepard, K. L.; Hone, J. *Nat. Nanotechnol.* **2010**, *5*, 722–726.
- (25) Das, A.; Pisana, S.; Chakraborty, B.; Piscanec, S.; Saha, S. K.; Waghmare, U. V.; Novoselov, K. S.; Krishnamurthy, H. R.; Geim, A. K.; Ferrari, A. C.; Sood, A. K. *Nat. Nanotechnol.* **2008**, *3*, 210–215.
- (26) Sundaram, R. S.; Steiner, M.; Chiu, H. Y.; Engel, M.; Bol, A. A.; Krupke, R.; Burghard, M.; Kern, K.; Avouris, P. *Nano Lett.* **2011**, *11*, 3833–3837.
- (27) Xiao, Y.; Francescato, Y.; Giannini, V.; Rahmani, M.; Roschuk, T. R.; Gilbertson, A. M.; Sonnefraud, Y.; Mattevi, C.; Hong, M. H.; Cohen, L. F.; Maier, S. A. *Phys. Chem. Chem. Phys.* **2013**, *15*, 5395–5399.
- (28) Fann, W. S.; Storz, R.; Tom, H. W. K.; Bokor, J. *Surf. Sci.* **1993**, *283*, 221–225.
- (29) Johannsen, J. C.; Ulstrup, S.; Cilento, F.; Crepaldi, A.; Zaccagna, M.; Cacho, C.; Turcu, I. C. E.; Springate, E.; Fromm, F.; Raidel, C.; Seyller, T.; Parmigiani, F.; Grioni, M.; Hofmann, P. *Phys. Rev. Lett.* **2013**, *111*, 027403.
- (30) Abb, M.; Albella, P.; Aizpurua, J.; Muskens, O. L. *Nano Lett.* **2011**, *11*, 2457–2463.
- (31) Hale, P. J.; Horne, S. M.; Moger, J.; Horsell, D. W.; Hendry, E. *Phys. Rev. B* **2011**, *83*, 121404(R).
- (32) Ruzicka, B. A.; Wang, S.; Liu, J. W.; Loh, K. P.; Wu, J. Z.; Zhao, H. *Opt. Mater. Express* **2012**, *2*, 708–716.
- (33) Wang, H. N.; Strait, J. H.; George, P. A.; Shivaraman, S.; Shields, V. B.; Chandrashekhara, M.; Hwang, J.; Rana, F.; Spencer, M. G.; Ruiz-Vargas, C. S.; Park, J. *Appl. Phys. Lett.* **2010**, *96*, 081917.
- (34) Tielrooij, K. J.; Song, J. C. W.; Jensen, S. A.; Centeno, A.; Pesquera, A.; Elorza, A. Z.; Bonn, M.; Levitov, L. S.; Koppens, F. H. L. *Nat. Phys.* **2013**, *9*, 248–252.
- (35) Winzer, T.; Knorr, A.; Malic, E. *Nano Lett.* **2010**, *10*, 4839–4843.
- (36) Ren, M. X.; Plum, E.; Xu, J. J.; Zheludev, N. I. *Nat. Commun.* **2012**, *3*, 833.
- (37) Malic, E.; Winzer, T.; Bobkin, E.; Knorr, A. *Phys. Rev. B* **2011**, *84*, 205406.
- (38) Hodak, J. H.; Henglein, A.; Hartland, G. V. *J. Chem. Phys.* **1999**, *111*, 8613–8621.
- (39) Fang, Z. Y.; Wang, Y. M.; Liu, Z.; Schlather, A.; Ajayan, P. M.; Koppens, F. H. L.; Nordlander, P.; Halas, N. J. *ACS Nano* **2012**, *6*, 10222–10228.
- (40) Freitag, M.; Low, T.; Xia, F. N.; Avouris, P. *Nat. Photonics* **2013**, *7*, 53–59.